Nanoscale

ROYAL SOCIETY OF CHEMISTRY

PAPER

View Article Online
View Journal | View Issue

Cite this: *Nanoscale*, 2025, **17**, 18633

Facile synthesis of magnetic core–shell structures for tunable microwave absorption†

Jiao Liu,[a] Xukang Han,[a] Wenjuan Ren,[a] Longqiang Liang,[b] Xiyao Wang,[a] Di Lan,[c] Mingliang Ma *[a] and Shengtao Gao*[d]

The rapid development of electronic communication and radar technologies in the 5G era has exacerbated electromagnetic pollution, thereby driving the urgent need for cutting-edge microwave absorption materials. In this study, a novel SnCo/C@MoS_2 composite was proposed, and the core–shell structure was synthesized *via* electrospinning and hydrothermal methods. This composite uniquely integrated the high conductivity and magnetic properties of Sn and Co while capitalizing on the superior dielectric performance of MoS_2 nanosheets, which are uniformly grown on carbon nanofibers. This design capitalized on the synergistic effects of a one-dimensional (1D) carbon fiber (CF) framework and two-dimensional (2D) MoS_2 nanostructures, enhancing interfacial polarization and multi-loss mechanisms. SnCo/C@MoS_2 exhibited remarkable microwave absorption properties, achieving a minimum reflection loss (RL_{min}) of −64.27 dB at a thickness of 1.52 mm and an effective absorption bandwidth (EAB) of 5.20 GHz. Moreover, computer simulation technology (CST) demonstrated that SnCo/CNF@MoS_2 simulated radar cross-section (RCS) values fell below −20 dB m^2. These results demonstrated a substantial improvement in absorption performance compared to the individual SnCo/CNF and MoS_2 components. This work underscored the effectiveness of combining 1D and 2D materials to obtain core–shell structures for superior electromagnetic wave (EMW) attenuation.

Received 21st March 2025,
Accepted 22nd April 2025

DOI: 10.1039/d5nr01174d

rsc.li/nanoscale

1. Introduction

With the advent of the 5G era, electronic communication and radar detection technologies are widely used in both civilian and military fields, significantly improving quality of life.[1] However, the widespread use of high-frequency electronic equipment generates EMWs that may pose a serious threat to human health and communication security, leading to a new form of pollution. This issue has attracted widespread societal attention. Air pollution, water pollution, noise pollution, and electromagnetic radiation are now defined as the four major sources of pollution. Consequently, the demand for electromagnetic shielding and microwave absorption materials is increasing. Currently, there are two primary methods to address electromagnetic pollution: electromagnetic shielding and electromagnetic absorption, with the latter being the most effective.[2–4] Therefore, extensive research on EMW-absorbing materials is urgently needed.

Carbon materials, such as carbon nanofibers (CNFs),[5] carbon nanotubes (CNTs)[6] and graphene,[7] are typical dielectric loss absorbers. In particular, CNFs offer unique advantages in 1D wave absorption due to their high specific surface area, low density, high aspect ratio, and stable chemical properties.[8] A simple and efficient electrospinning technique is typically employed to produce stable magnetic CF. While CNF materials loaded with a single magnetic metal have been extensively studied, their loss mechanism remains relatively simple, leading to suboptimal impedance matching and inadequate EMW attenuation. Consequently, combining lightweight carbon-based materials with various magnetic absorbers can diversify loss mechanisms and improve impedance matching to some extent. Common magnetic absorbing materials include magnetic metal powders, metal oxides, and ferrites. Zhang *et al.* prepared multi-phase carbon-coated $FeSn_2$/Sn nanocomposites by an *in situ* arc discharge method and achieved effective absorption across the 9–18 GHz range.[9] Hu *et al.* prepared CoNi/C nanofibers with excellent absorption properties by adjusting the ratio of Co and Ni. When the Co/Ni ratio was 1/3, the matching thickness was 2.4 mm and the RL_{min} was −71.2 dB. In addition, the maximum EAB (EAB_{max})

[a]*School of Civil Engineering, Qingdao University of Technology, Qingdao 266520, People's Republic of China. E-mail: mamingliang@qut.edu.cn*
[b]*Qingdao Shamu New Material Co., Ltd, Qingdao 266113, People's Republic of China*
[c]*School of Materials Science and Engineering, Hubei University of Automotive Technology, Shiyan 442002, P.R. China*
[d]*School of Chemical Engineering and Blasting, Anhui University of Science and Technology, Anhui 232001, People's Republic of China. E-mail: shtgao@aust.edu.cn*
† Electronic supplementary information (ESI) available. See DOI: https://doi.org/10.1039/d5nr01174d

reached 5.9 GHz, covering the entire Ku band.[10] Shen *et al.* showed that $NiFe_2O_4$/NiO/CNF exhibited an EAB of 8 GHz when the load in paraffin was 50%, and the content of FeNi/$NiFe_2O_4$/NiO/CNF in paraffin was only 5%, with an RL_{min} of −37.4 dB at 12.8 GHz. However, the EAB of 4.3 GHz was narrowed.[11] Therefore, the combined use of CF and a variety of magnetic absorbing materials is insufficient to further improve the EMW absorption performance and broaden the effective absorption bandwidth.

2D layered nanostructured materials (TDMs) like graphene,[12] black phosphorus,[13] MoS_2,[14] WS_2,[15] and MXene[16] have gained significant attention as potential next-generation microwave absorbers due to their lightweight, strong absorption coefficients, and thin structures. Among these, MoS_2 stands out due to its low cost, high specific surface area, and unique electrical and optical properties, making it particularly promising for electromagnetic attenuation in electronic and optoelectronic devices.[17,18] Its exceptional photoelectric properties enhance conductive and polarization losses, leading to superior attenuation performance and impedance matching compared to traditional carbon-based dielectric materials. Sun *et al.* regulated the microwave absorption performance of MoS_2 by constructing various microscopic interface structures, finding that different van der Waals heterogeneous structures yielded distinct absorption characteristics. Notably, 2D MoS_2/3D carbon layers achieved an RL_{min} of −69.2 dB with an EAB of 4.88 GHz.[19] Similarly, Xu *et al.* enhanced absorption by coating hollow carbon spheres (MHCSs) with a MoS_2 layer, forming core–shell nanospheres (MHCS@MoS_2) that provided an EAB of 6.21 GHz at a matching thickness of 2.1 mm.[20] Zhao *et al.* spun Mil88 A into CNFs by electrospinning and grew MoS_2 on the surface of CF, which formed a nanorod heterostructure with a magnetic flower shape (CF-Mil88 A@MoS_2) with an RL of −70 dB at a thickness of 2.5 mm and an EAB of 4.68 GHz.[21] Although previous studies have investigated composites of magnetic and dielectric materials for EMW absorption, achieving strong absorption, broad bandwidth, and lightweight structures simultaneously remains challenging. This study addresses these limitations by designing a core–shell SnCo/C@MoS_2 composite that exploits the synergistic effects of 1D/2D hybrid structures to enhance EMW attenuation.

Based on the favorable magnetic properties of Sn and Co and the excellent electrical conductivity of MoS_2, this paper employs highly conductive CF as the base of Sn and Co and wraps a layer of MoS_2 on the fiber surface, thereby combining the morphological advantages of 1D CNFs with the unique nanostructure of the 2D material MoS_2. SnCo/C@MoS_2 is prepared, its microstructure and electromagnetic properties are studied, and the mechanism of synergistic enhancement of the absorbing properties of Sn, Co and MoS_2 composites is discussed.

2. Experimental section

2.1 Materials

Stannous chloride dihydrate ($SnCl_2{\cdot}2H_2O$, 99%, Sinopharm Chemical Reagent Co., Ltd (SCRC)), cobalt nitrate hexahydrate ($Co(NO_3)_2{\cdot}6H_2O$, 99%, SCRC), *N*,*N*-dimethylformamide (DMF, 99.5%, SCRC), sodium molybdate dihydrate ($Na_2MoO_4{\cdot}2H_2O$, 99%, SCRC), thioacetamide (C_2H_5NS, 99%, SCRC) and polyacrylonitrile (PAN, M_w = 150 000, Shanghai Aladdin Bio-Chem. Technology Co., Ltd).

2.2 Synthesis of SnCo/C@MoS_2

2.2.1 Synthesis of SnCo/CNF. A mixture of 1.6 g PAN and 18 mL DMF was magnetically stirred at 70 °C for 12 h, followed by the addition of 1 mmol $SnCl_2{\cdot}2H_2O$ and 1 mmol $Co(NO_3)_2{\cdot}6H_2O$ and stirring for another 12 h to form the precursor solution. SnCo/PAN fibers were obtained through electrospinning and then collected and dried at 50 °C for 10 h. SnCo/CNF was obtained by pre-carbonizing the dried SnCo/PAN at 280 °C for 2 h to stabilize the fiber structure and carbonizing at 800 °C for 3 h under a nitrogen atmosphere. Sn/CNF and Co/CNF were also prepared as control samples.

2.2.2 Synthesis of SnCo/C@MoS_2. C_2H_5NS (0.64 g) and $Na_2MoO_4{\cdot}2H_2O$ (0.32 g) were dissolved in 80 mL deionized water, stirred magnetically for 1 h, and then 0.2 g SnCo@CNF nanofibers were dispersed in the solution and reacted at 200 °C for 24 h. The mixture was centrifuged and washed with ethanol and deionized water three times each. The resulting precipitate was freeze-dried to obtain SnCo/C@MoS_2. It should be noted that Sn/CNF, Co/CNF, SnCo/CNF, and SnCo/C@MoS_2 were referred to as SC, CC, SCC, and SCCM, respectively.

2.3. Characterization

The surface morphology and micro-composition of the materials were analyzed using a scanning electron microscope (SEM, Sigma 300) coupled with a scanning energy dispersive spectrometer (EDS). The crystal structure was analyzed using an X-ray diffractometer (XRD, Shimadzu XRD-7000). The degree of graphitization was characterized by Raman spectroscopy (Thermo DXR2). Fourier transform infrared spectroscopy (FTIR, Shimadzu IRTracer 100) was used to detect the chemical bonds in the molecules and analyze the molecular structure characteristics of the samples. X-ray photoelectron spectroscopy (XPS, Thermo Scientific Nexsa) was used to characterize the chemical composition and valence state of the material. Static magnetic properties were measured using a vibrating sample magnetometer (VSM, Lake Shore 7307). The electromagnetic parameters of the samples prepared as paraffin rings (2–18 GHz) were analyzed using a vector network analyzer (VNA, Agilent A N5244A).

3. Results and discussion

3.1. Microstructure and component

The synthesis process of SnCo/C@MoS_2 by electrospinning and hydrothermal techniques is shown in Fig. 1a. Electrospinning produced 1D CNFs as the matrix, which interwove with each other to form a three-dimensional (3D) conductive network with magnetic particles loaded onto the CNF.[22] Hydrothermal growth of 2D nanosheets onto the fiber surface

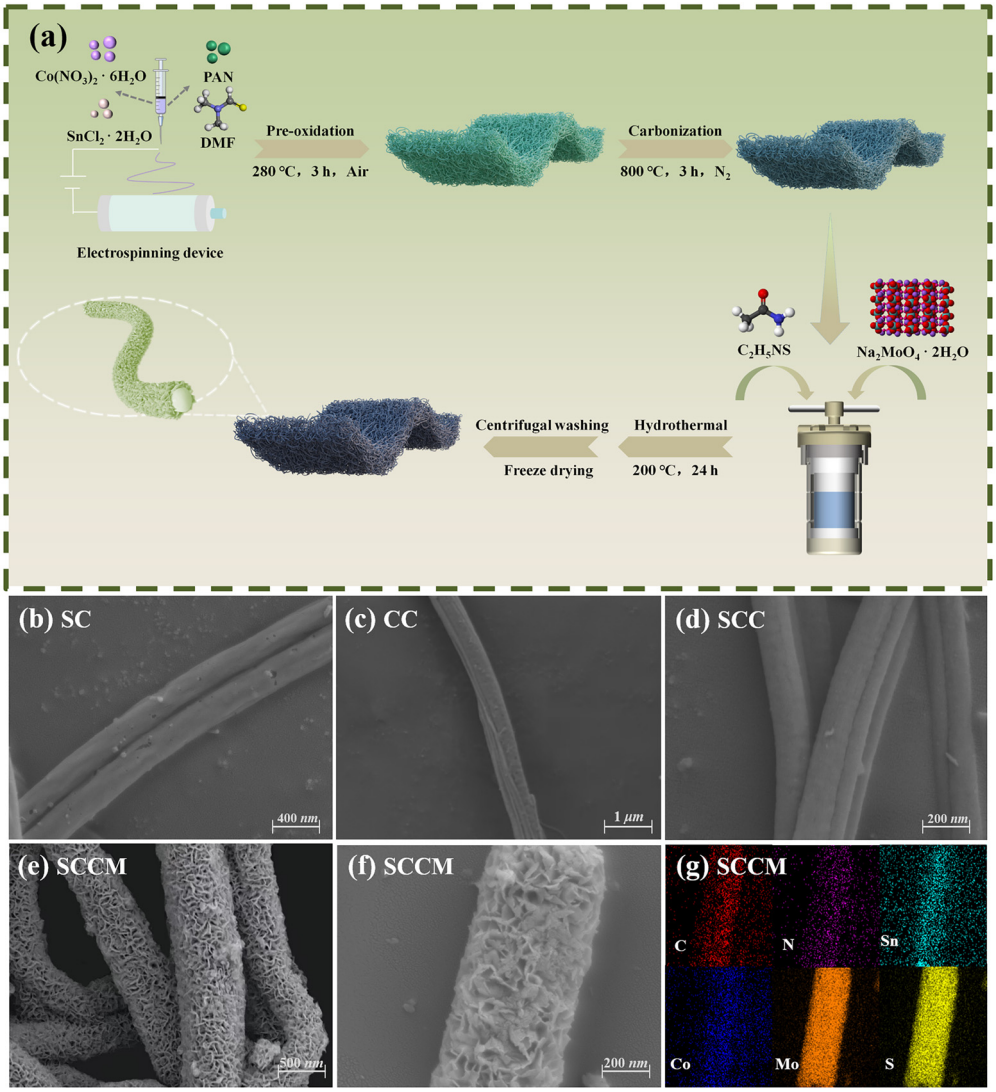

Fig. 1 Schematic of the preparation process of SCCM (a); SEM of SC (b), CC (c), SCC (d) and SCCM (e and f); elemental mapping analysis of SCCM (g).

forming a core–shell structure lengthened the multiple reflection loss paths. In Fig. 1b–g, SEM images of SC, CC, SCC and SCCM and EDS spectra of SCCM are shown. Observation of the morphological features of SC and CC samples (Fig. 1b, c and Fig. S1a†) revealed that Sn and Co particles made the surface of CNF rough. As can be seen from Fig. 1d, small bumps were uniformly distributed on the surface of CNF, a result of the nanoscale SnCo alloy being anchored on the surface of CNF. Fig. S1b† clearly displays the SnCo alloy topography of SCC. Fig. S1c–f† show the distribution of elements C, N, Sn and Co of SCC respectively, where Sn and Co were uniformly distributed, indicating the existence of SnCo alloys. Fig. 1e and f clearly demonstrate the successful growth of MoS_2 nanosheets to form core–shell structures on the SCC fiber surface. The large specific surface area of MoS_2 nanosheets can prolong the reflection path of EMWs, and the high dielectric properties of MoS_2 were conducive to conductive losses. Fig. 1g shows the EDS diagram of SCCM (Fig. 1f) with a uniform distribution of C, N, Sn, Co, Mo and S elements, proving that SnCo/C@MoS_2 was successfully prepared.[23] Furthermore, the similar distribution patterns of Sn with Co and Mo with S underpin the formation of the SnCo alloy and MoS_2.

XRD patterns of SC, CC, SCC, and SCCM samples and PDF cards of SnCo alloys and MoS_2 are shown in Fig. 2a. The SC sample had obvious peaks at 2θ of 30.64°, 32.02° and 44.90°, corresponding to the (200), (101) and (211) crystal faces of Sn, respectively. The CC sample had obvious peaks at 44.22°, 51.52°, and 75.85°, corresponding to the (111), (200), and (220) crystal faces of Co, respectively. In addition, SC and CC had gentle peaks at 2θ of 25°, indicating that PAN fibers were directly transformed into amorphous carbon during carbonization.[24] The SCC sample had peaks at 2θ of 28.49°, 33.93°, 45.07°, 55.66°, 57.56°, and 71.40°, representing the (101),

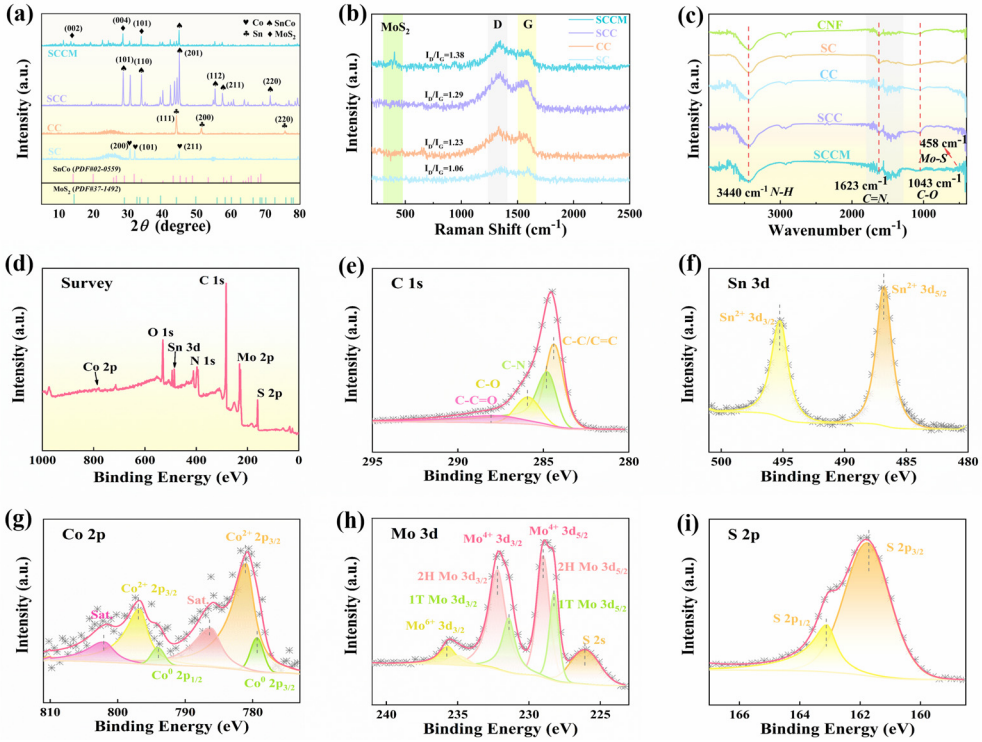

Fig. 2 XRD pattern (a); Raman spectrum (b); FTIR spectra of SC; CC, SCC and SCCM (c); XPS survey spectra (d), C 1s (e), Sn 3d (f), Co 2p (g), Mo 3d (h) and S 2p (i) of SCCM.

(110), (201), (112), (211), and (220) crystal faces of the SnCo alloy (PDF#02-0559), respectively. SCCM corresponded to the (002), (004) and (101) crystal faces of MoS_2 (PDF#37-1492) at 2θ of 14.37°, 29.02° and 33.51°, respectively.[25] As a result, a portion of Sn and Co formed an SnCo alloy, and a (002) crystal face appeared in the SCCM at 14.37°, which meant that MoS_2 was successfully coated on the SCC surface, in contrast to the SCC.

The degree of graphitization in carbon materials affected their electromagnetic parameters and microwave absorption properties.[26] Thus, analyzing graphitization through Raman spectroscopy was necessary.[27] Fig. 2b displays the Raman spectra of the samples, all of which exhibited strong vibration peaks at the D band (1349 cm^{-1}) and G band (1587 cm^{-1}), corresponding to lattice defects in graphite carbon atoms and the tensile vibration of sp^2 hybridized carbon, respectively.[28] The I_D/I_G ratio reflected the degree of graphitization, with a higher I_G peak indicating greater graphitization. In Fig. 2b, the I_D/I_G ratios for SC, CC, SCC, and SCCM were 1.06, 1.23, 1.29, and 1.38, respectively. Obviously, the degree of graphitization decreased successively, and it is worth mentioning that the degree of graphitization was the lowest in the SCCM sample, which was attributed to the large number of defects brought about by the introduction of MoS_2. In addition, SCCM exhibited two small peaks at 370 cm^{-1} and 400 cm^{-1} that are characteristic peaks of MoS_2, which are attributed to the first-order Raman vibration mode of S.[29] The edge termination structure at 400 cm^{-1} was dominant, which was conducive to electron transition and increased conductive loss.[30]

The bonding mode was interpreted using infrared spectroscopy. The characteristic absorption peaks of CNF, SC, CC, SCC and SCCM are shown in Fig. 2c. A prominent absorption peak at 3340 cm^{-1} corresponded to the stretching vibrations of O–H, N–H, or C–H bonds, confirming the presence of hydrogen bonds within the material. A subtle peak around 1623 cm^{-1} was attributed to C=N stretching, originating from the vibrations of C–N and C=C bonds within the benzene ring. The absorption peak at 1043 cm^{-1} was associated with the single bond vibration of C–O. In addition, the peak at 458 cm^{-1} in SCCM, attributed to Mo–S vibrations, confirmed the successful growth of MoS_2 on the SCC surface.[31]

The XPS analysis of the chemical states of C, Sn, Co, Mo, and S in SCCM samples is presented in Fig. 2d–i. The full spectrum of the SCCM sample is shown in Fig. 2d. Fig. 2e depicts four fitting peaks of C 1s, corresponding to distinct bonding states including C–C/C=C (284.8 eV), C–N (285.0 eV), C–O (285.9 eV), and C–C=O (288.1 eV).[32,33] The presence of the C–C=O bond indicated oxygen involvement during PAN pyrolysis to form carbon. In Fig. 2f, the Sn 3d spectrum exhibited two symmetric peaks, assigned to Sn^{2+} $3d_{5/2}$ (486.8 eV) and Sn^{2+} $3d_{3/2}$ (495.3 eV) states.[34] Fig. 2g shows that the Co 2p spectrum comprises six peaks, indicating the presence of Co in two oxidation states, Co^0 and Co^{2+}. Co^0 $2p_{3/2}$ and Co^0 $2p_{1/2}$ peaks appeared at binding energies of 779.4 eV and 794.1 eV, respectively, while Co^{2+} $2p_{3/2}$ and Co^{2+} $2p_{1/2}$ were observed at 781.1 eV and 796.9 eV. Additionally, satellite peaks (Sat.) were located at 785.4 eV and 802.1 eV.[35,36] In Fig. 2h, the deconvoluted Mo 3d

spectrum confirmed the presence of Mo in multiple valence states (Mo^0, Mo^{4+}, and Mo^{6+}) and the coexistence of 1T and 2H phases in SCCM. Peaks at 228.3 eV (Mo $3d_{5/2}$) and 231.4 eV (Mo $3d_{3/2}$) corresponded to the metallic 1T phase of MoS_2,[37] while those at 228.9 eV (Mo $3d_{5/2}$) and 232.2 eV (Mo $3d_{3/2}$) represented the semiconducting 2H phase.[38,39] In Fig. 2i, binding energies at 226.1 eV (S 2s) and 235.8 eV (Mo^{6+} $3d_{3/2}$) indicated the formation of Mo–S bonds and partial oxidation of MoS_2 to Mo^{6+}.[40] The S 2p spectrum was deconvoluted into two peaks, S $2p_{3/2}$ (161.7 eV) and S $2p_{1/2}$ (163.1 eV), confirming that MoS_2 grew on the CNF surface.[41]

3.2. Magnetic performance

Magnetostatic analysis (VSM) was performed on SC, CC, SCC and SCCM samples in order to understand the magnetic properties of the samples in depth, as shown in Fig. 3 and Table 1. Under external magnetic fields of −30 000 to 30 000 Oe, the hysteresis loops of SC, CC, SCC and SCCM samples exhibit a typical S-shape (Fig. 3a), indicating that the magnetization reached a saturation state, which led to favorable magnetic losses.[42] It can be seen from Table 1 that the saturation magnetization (M_s) values of CC, SCC and SCCM samples were 25.06, 9.08 and 6.20 emu g^{-1}, respectively (where SC was not magnetic). The M_s values of SCC and SCCM decreased in turn, due to the non-magnetic Sn loading on the CNF and the non-magnetic MoS_2 coating on the SCC fiber surface.[43,44] In Fig. 3b, the remanent magnetization (M_r) values of CC, SCC and SCCM samples were 6.22, 2.35 and 1.57 emu g^{-1}, respectively. High coercivity (H_c) meant high magnetic anisotropy. The H_c of the SCCM sample was 190.90 Oe, higher than those of CC and SCC (114.56 and 167.89 Oe), indicating that SCCM had prominent magnetic anisotropy, which increased the demagnetization energy and prevented the reversal of magnetic domains.

Table 1 M_s, M_r and H_c of SC, CC, SCC and SCCM

Samples	M_s (emu g^{-1})	M_r (emu g^{-1})	H_c (Oe)
SC	—	—	—
CC	25.06	6.22	114.56
SCC	9.08	2.35	167.89
SCCM	6.20	1.57	190.90

3.3. Microwave property analysis

3.3.1 Microwave absorption performance. Based on transmission line theory,[45] the EMW absorption properties of materials can be assessed through impedance (Z_{in}) and RL, both in the medium and in free space, as shown in eqn (1) and (2):

$$Z_{in} = Z_0\sqrt{\frac{\mu_r}{\varepsilon_r}}\tanh\left[j\frac{2\pi fd}{c}\sqrt{\mu_r\varepsilon_r}\right] \quad (1)$$

$$RL = 20\lg\left|\frac{Z_{in}-Z_0}{Z_{in}+Z_0}\right|. \quad (2)$$

In the formula, Z_0 represents the air impedance, μ_r denotes the relative permeability, ε_r signifies the relative dielectric constant, f indicates the incident EMW frequency (Hz), d refers to the sample thickness (mm), and c stands for the speed of light in a vacuum.[46] When evaluating the performance of EMW absorbing materials, the primary index used was RL. The RL of −10 dB indicated that 90% of the EMW was absorbed, while RL < −10 dB corresponded to the EAB of the material.[47] As shown in Fig. 4a–d, the RL_{min} of SC was −28.85 dB (10.94 GHz, d = 2.13 mm), and the EAB_{max} was 4.73 GHz (13.28–18 GHz, d = 1.5 mm). As shown in Fig. 4e–h, the RL_{min} of CC was −20.61 dB (7.42 GHz, d = 2.79 mm), and the EAB_{max} was 5.04 GHz (12.96–18 GHz, d = 1.58 mm). Sample SC primarily absorbed X and Ku-band EMWs, while CC absorbed C, X, and Ku-band waves, offering broader coverage and a larger EAB than SC, mainly due to the presence of cobalt as a magnetic element. However, despite its wave-absorbing properties, CC exhibited unsatisfactory thickness and RL values. By preparing bimetallic CF SnCo/C, we aimed to address the issues of excessive thickness and low RL values. As illustrated in Fig. 4i–l, SCC exhibited an RL_{min} of −59.49 dB (4.74 GHz, d = 5.67 mm) and an EAB_{max} of 4.94 GHz (7.02–11.96 GHz, d = 3.1 mm). While the RL of SCC required significant enhancement, it

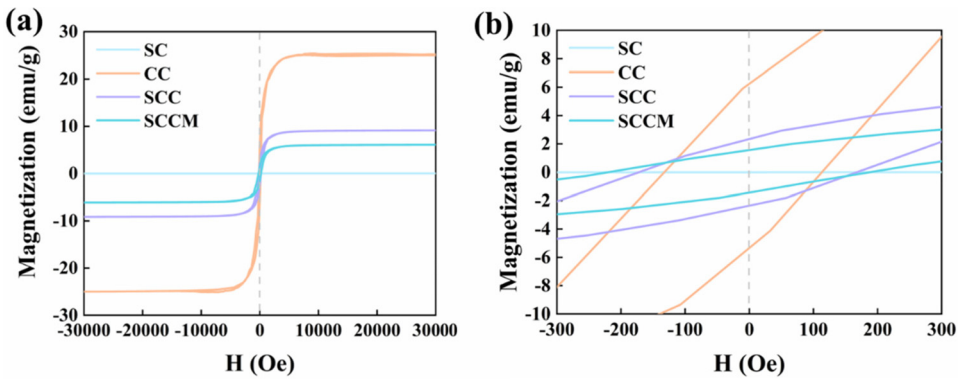

Fig. 3 Hysteresis loops (a) of SC, CC, SCC, and SCCM and enlarged view of hysteresis loops (b).

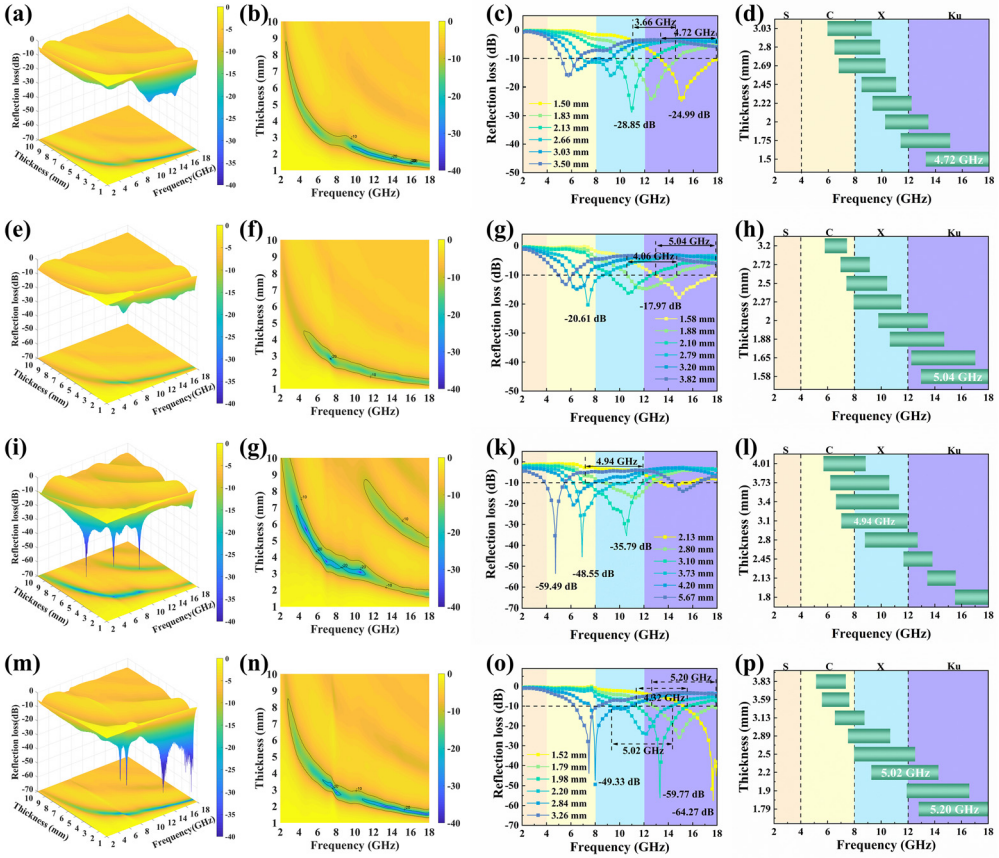

Fig. 4 3D and 2D RL and EAB curves of SC (a–d), CC (e–h), SCC (i–l) and SCCM (m–p).

paradoxically resulted in increased thickness. Remarkably, incorporating high-conductivity MoS_2 onto the SnCo/CNF surface enabled the attainment of reduced thickness alongside heightened attenuation.[48] Fig. 4m–p illustrates the presence of three prominent absorption peaks at thicknesses of 1.52 mm, 1.98 mm, and 2.84 mm, corresponding to RL values of −64.27 dB (17.68 GHz), −59.77 dB (13.32 GHz), and −49.33 dB (8.00 GHz), respectively, with EAB surpassing 3.2 GHz. Notably, Fig. 4p indicates that the absorption band of SCCM spanned the entire 2–18 GHz range. A longitudinal comparison of the EAB between SCC and SCCM, as demonstrated in Fig. 4l and p, revealed that while the EAB of SCC was primarily centered around the X-band, the EAB of SCCM extended significantly into higher frequency regions, encompassing the entire X and Ku bands and exceeding 5 GHz in this spectrum, attributed to the elevated conductivity of magnetic metals Co and MoS_2. Table 2 displays RL_{min}, corresponding thickness at RL_{min} (dRL_{min}), and EAB values. Through comparison, it was evident that the SCC coated with a MoS_2 layer in this study achieved commendable RL_{min}, thickness, and EAB, with the SCCM fiber demonstrating outstanding EMW absorption capabilities. As indicated in Table 2, the fabricated SCCM nanofibers exhibited minimal thickness (1.52 mm), excellent RL_{min} (−64.27 dB), and relatively high EAB (5.20 GHz). In accordance with the current trends in microwave absorption materials, key attributes included "thin thickness, light weight, broad bandwidth, and high loss".[49]

Table 2 Recent research on MoS_2 composites and their EMW absorption performance

Sample	RL_{min} (dB)	dRL_{min} (mm)	EAB (GHz)	Ref.
MoS_2/Ni	−44.70	2.60	2.8	50
CNT@MoS_2	−66.80	1.60	4.8	51
Co/CoS_2@NC@MoS_2	−43.90	3.50	4.40	52
CoZn/C@ MoS_2	−41.50	4.50	4.58	53
MoS_2@C@$CoFe_2O_4$	−47.70	2.40	3.50	54
$CoFe_2O_4$@1T/2H-MoS_2	−68.5	1.81	4.56	55
MoS_2/CoNi	−41.44	2.00	5.60	56
$Co_3SnC_{0.7}$/CNF	−21.7	2.00	5.92	57
SCCM	−64.27	1.52	5.20	This work

3.3.2. Electromagnetic parameters and absorption mechanism. Analyzing the electromagnetic characteristic parameters enabled the evaluation of a material's response capability and absorption performance under EMWs.[58] The two fundamental parameters characterizing the electromagnetic properties of materials—complex permittivity (ε_r) and complex permeability

(μ_r)—were employed to assess the attenuation capacity of EMWs, as shown below (eqn. (3)–(6)):

$$\varepsilon_r = \varepsilon' - j\varepsilon'' \quad (3)$$

$$\mu_r = \mu' - j\mu'' \quad (4)$$

$$\tan\delta_\varepsilon = \frac{\varepsilon''}{\varepsilon'} \quad (5)$$

$$\tan\delta_\mu = \frac{\mu''}{\mu'} \quad (6)$$

In electromagnetism, the real component of the dielectric constant (ε') reflected a material's ability to store electromagnetic energy, whereas the imaginary component (ε'') denoted its ability to absorb and dissipate energy. The real and imaginary components of magnetic permeability (μ) corresponded to the material's energy storage density and its magnetic dissipation capability, respectively. The dielectric loss angle tangent ($\tan\delta_\varepsilon$) and magnetic loss angle tangent ($\tan\delta_\mu$) were employed to assess the material's dissipative properties.[59] Fig. 5 depicts the changes in electromagnetic parameters (ε', ε'', μ', and μ'') and the corresponding tangents of electromagnetic loss for both SCCM and SCC. As seen in Fig. 5a and c, ε' exhibited a declining trend as frequency increased. For example, the ε' of SCC decreased from 8.68 GHz to 6.13 GHz, and SCCM decreased from 12.97 GHz to 7.27 GHz. This can be attributed to the dispersion effect, where the displacement current in an alternating electric field failed to keep pace with the accumulated potential.[60] The permeability (μ) of SCCM was comparatively lower than that of SCC, as MoS_2 nanosheets were non-magnetic, and their incorporation dilutes the magnetic properties of SCC. A comparison of Fig. 5b and d showed that the $\tan\delta_\varepsilon$ for SCC fluctuated around 0.3, while SCCM fluctuated around 0.5, indicating that SCCM had superior electrical conductivity, which was attributed to the unique structure of MoS_2 inducing electrons to move along the 3D network of CNF. This resulted in conductive loss.[61] The SCCM sample exhibited a peak at 10 GHz, which was attributed to interfacial

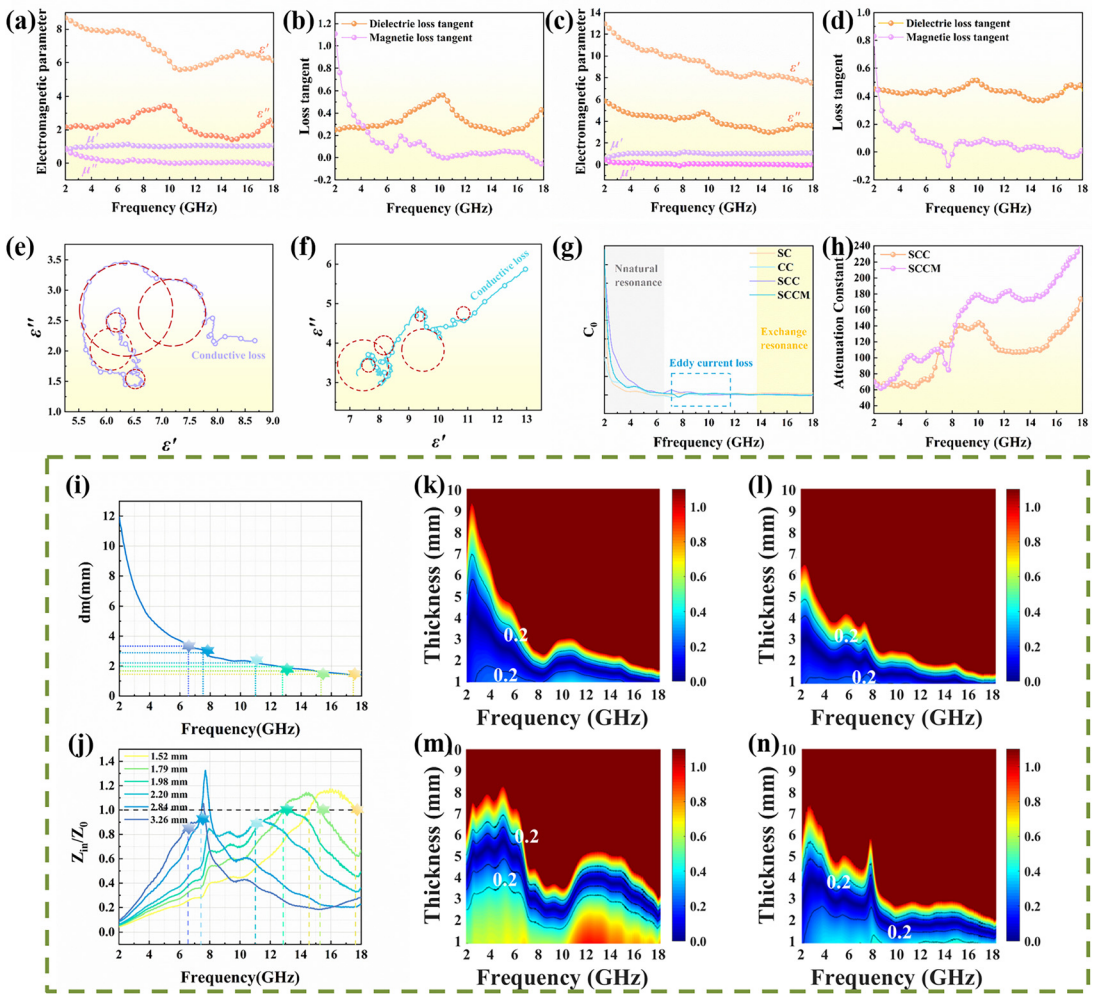

Fig. 5 Electromagnetic parameters of SCC (a) and SCCM (c) and the loss tangent of SCC (b) and SCCM (d); Cole–Cole of SCC (e) and SCCM (f); C_0 curve diagram (g); attenuation constant (h); 1/4 wavelength matching (i) and 2D Z curves of SCCM (j); colorful contour maps of $|\Delta|$ for SC (k), CC (l), SCC (m) and SCCM (n).

polarization arising from the differing conductive properties of MoS_2 and SnCo/CNF. As shown in Fig. 5b, 4 GHz marked the turning point: below this frequency, the tangent of $\tan\delta_\mu$ exceeded that of $\tan\delta_\varepsilon$, indicating magnetic loss as the dominant mechanism. Above 4 GHz, the electrical loss became dominant. As depicted in Fig. 5d, the SCCM sample consistently showed a higher $\tan\delta_\varepsilon$ compared to the $\tan\delta_\mu$ across the 2–8 GHz frequency range, suggesting that electrical loss was the dominant mechanism throughout the microwave phase. This was attributed to the incorporation of high-dielectric MoS_2.

In the microwave phase, the primary polarization types were interface and dipole polarization, with the Cole–Cole curve employed to elucidate the polarization mechanism in detail (eqn (7) and (8)). Each semicircle represented a Debye polarization relaxation, with more complex semicircles indicating a greater number of relaxation types within the material,[62,63] resulting in stronger polarization loss. There were long linear tails indicating conductive losses.

$$\left(\varepsilon' - \frac{\varepsilon_s - \varepsilon_\infty}{2}\right)^2 + (\varepsilon'')^2 = \left(\frac{\varepsilon_s - \varepsilon_\infty}{2}\right)^2 \quad (7)$$

$$\varepsilon' = \varepsilon_\infty + \frac{1}{\tau}\left(\frac{\varepsilon''}{\omega}\right) \quad (8)$$

The parameters ε_s, ε_∞, τ, and ω in the above formula corresponded to the low-frequency electrostatic permittivity, high-frequency relative permittivity, relaxation time, and angular frequency, respectively. The Cole–Cole curves for SC, CC, SCC, and SCCM are shown in Fig. S2a and b† and Fig. 5e and f. It was evident that dual loss mechanisms, namely polarization relaxation and conduction loss, were present. With the addition of Co, Sn, and MoS_2 to CNF, the number of semicircles increased, among which SCCM had the most semicircles compared with other samples, indicating that SCCM samples had more diverse relaxation types and stronger loss capacity to EMWs, which was attributed to the formation of new heterostructures after the introduction of high-dielectric MoS_2 (MoS_2–CNF). Interfacial polarization and dipole polarization can occur in many locations, including Co–Sn, Co–CNF, Sn–CNF, MoS_2–CNF, *etc.*[64] In addition, SCCM had an obvious long tail, suggesting that the sample not only had excellent polarization relaxation loss but also had strong conductive loss. The CNF, MoS_2, and SnCo metal particles generated induced currents when exposed to alternating electromagnetic fields, thereby transforming electromagnetic energy into heat and contributing to conductive loss. This dual-loss mechanism served as the basis for improving the EMW absorption capability of SCCM. The C_0 curve in Fig. 5g depicts the magnetic loss mechanisms including natural resonance, eddy current loss, and exchange resonance observed in SC, CC, SCC, and SCCM samples across the 2–18 GHz range.[65,66] Based on Aharoni's theory,[67] natural resonance primarily occurred at low frequencies, eddy current loss was observed in the mid-frequency range, and exchange resonance dominated at high frequencies. During the initial segment of the C_0 curve (2–6 GHz), all samples exhibited a distinct decline and fluctuation, suggesting the presence of natural resonance at low frequencies, attributed to the anisotropy induced by the small size of Sn and Co nanoparticles loaded onto the CNF.[68] In the mid- to high-frequency range of the C_0 curve (6–18 GHz), the C_0 value remained stable, indicating that eddy current loss and exchange resonance were the predominant mechanisms. Consequently, it can be inferred that the magnetic loss mechanism varies across frequency ranges, with all mechanisms contributing to the overall magnetic loss.

To better understand the EMW attenuation mechanism, the attenuation constant (α) was a critical evaluation parameter. The ability of the absorber to attenuate EMWs depended on the α, calculated as follows (eqn (9)):

$$\alpha = \frac{\sqrt{2}\pi f}{c} \times \sqrt{(\mu''\varepsilon'' - \mu'\varepsilon') + \sqrt{(\mu''\varepsilon'' - \mu'\varepsilon')^2 + (\mu'\varepsilon'' - \mu''\varepsilon')^2}} \quad (9)$$

The α values of SCC and SCCM are shown in Fig. 5h. It was evident that the α of SCCM exceeds that of SCC, indicating that EMWs underwent rapid attenuation upon entering the SCCM sample. In addition to the magnetic loss attributed to MoS_2, the introduction of MOS_2 enhanced interfacial polarization sites. In general, when ε_r was sufficiently large, an increase in μ_r led to a higher α, enhancing the material's attenuation capacity. However, an excessively high α could lead to impedance mismatch, as attenuation and impedance matching were inherently conflicting factors. Therefore, the real and imaginary components of ε_r and μ_r do not necessarily need to be maximized. Minimizing reflection was essential for achieving strong microwave absorption, which necessitated that the impedance ratio (Z) between the absorber and free space approached "1".[69] For materials incorporating both magnetic and dielectric components, the impedance matching design principle can be derived from the following equations (eqn (10)–(13)):

$$Z = \left|\frac{Z_{in}}{Z_0}\right| = \sqrt{\left|\frac{\mu_r}{\varepsilon_r}\right|} = \sqrt{\frac{\sqrt{\mu''^2 + \mu'^2}}{\sqrt{\varepsilon''^2 + \varepsilon'^2}}} \quad (10)$$

$$|\Delta| = |\sinh^2(Kfd) - M| \quad (11)$$

$$K = \frac{4\pi\sqrt{\varepsilon_r'\mu_r'}\sin\left(\frac{\delta_\varepsilon + \delta_\mu}{2}\right)}{c \cdot \cos\delta_\varepsilon \cos\delta_\mu} \quad (12)$$

$$M = \frac{4\mu' \cos\delta_\varepsilon \varepsilon' \cos\delta_\mu}{(\mu'\cos\delta_\varepsilon - \varepsilon'\cos\delta_\mu)^2 + \left[\tan\frac{\delta_\mu - \delta_\varepsilon}{2}\right]^2 (\mu'\cos\delta_\varepsilon + \varepsilon'\cos\delta_\mu)^2} \quad (13)$$

According to quarter-wavelength theory, the matching thickness (d_m) decreases as frequency increases. The relationship between SCCM matching thickness and frequency is shown in Fig. 5i. In conjunction with Fig. 5j, the Z values of SCCM at matching thicknesses of 1.52 mm (17.78 GHz), 1.79 mm (15.26 GHz), 1.98 mm (12.85 GHz), and 2.84 mm (7.40 GHz) were 1, indicating good impedance matching.

Besides Z, the value of $|\Delta|$ can also be used to assess impedance matching. A smaller $|\Delta|$ signified improved impedance matching, with $|\Delta| < 0.2$ deemed excellent and adequate for meeting EMW absorption criteria. As illustrated in Fig. 5, a larger blue region indicated better impedance matching, with the SC, CC, and SCCM samples showing a larger blue area. Both SC and CC demonstrated good impedance matching within the 1.5–4.0 mm range, as well as RL < −20 dB within this thickness range. In Fig. 5m, the narrow blue area of SCC was prominent, with a larger thickness (3.5–4.5 mm), indicating that most EMWs were reflected at small thicknesses due to unmatched input impedance. Therefore, adding MoS_2 to adjust impedance matching was expected to create a synergistic effect between impedance matching and electromagnetic loss at a small matching thickness. Fig. 5n clearly shows that the blue area in SCCM spanned the entire microwave range, indicating excellent impedance matching. Additionally, SCCM exhibited good impedance matching in the thin range of 1–3.8 mm, with multiple strong absorption peaks (RL < −40 dB) within this range in Fig. 4o and an EAB around 5 GHz in Fig. 4p.

3.4. RCS simulation results

To evaluate the EMW absorption performance of SCCM in practical applications, CST, professional electromagnetic simulation software, was used to measure the RCS.[70–72] The loss mechanism was further analyzed using SC, CC, SCC, and SCCM as the absorption layer, with a perfect electric conductor (PEC) as the reflector (Fig. 6 and Fig. S4†). RCS represented a physical measurement of the intensity of the echo generated by a target under radar irradiation.[73] Therefore, the RCS value was small, and the absorption performance of the material was excellent. As shown in Fig. S4a,† pure PEC produced the largest electromagnetic scattering signal at 0°. As shown in Fig. 6c, when PEC was coated with the four different samples, the RCS value significantly decreased, demonstrating effective EMW dissipation. The PEC coated with the SCCM absorber demonstrated the lowest RCS value (below −20 dB m^2), reflecting superior EMW absorption, which aligned with the transmission line theoretical calculations. Fig. 6d presents a bar chart comparing RCS reductions across the four different materials at different angles. The RCS reductions for SCCM were 34.28 dB m^2 at 0° and 13.77 dB m^2 at 40°, confirming its excellent absorption properties and practical feasibility for microwave absorption applications. Overall, the superior RCS reduction and alignment with theoretical predictions confirm SCCM's practical feasibility as a high-performance microwave absorber, making it a promising candidate for advanced electromagnetic shielding and stealth applications in both military and civilian fields.

The absorbing performance and electromagnetic parameters of SCCM were thoroughly analyzed above. The potential electromagnetic loss mechanisms of SCCM are shown in Fig. 7. The introduction of high-dielectric MoS_2 and magnetic Co particles worked synergistically to balance the dielectric constant, achieving excellent impedance matching. First, interfacial polarization arose between metal particles (Sn–Co), between metal particles and CNF (Sn–CNF and Co–CNF), and

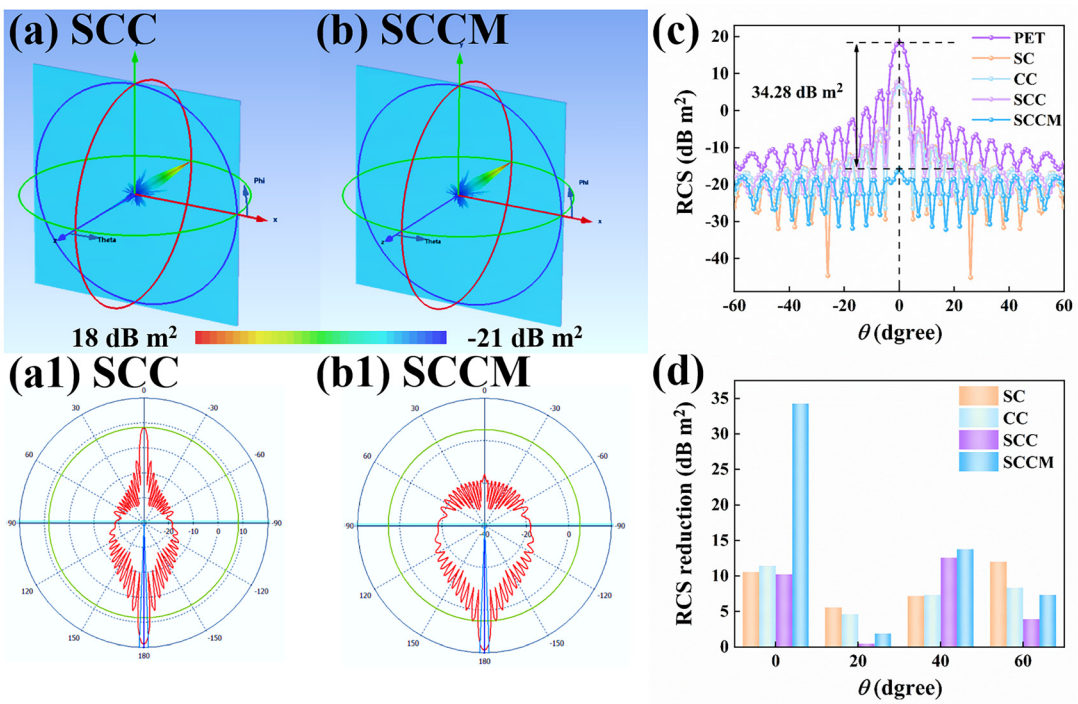

Fig. 6 RCS simulation images of SCC (a) and SCCM (b); RSC values of SCC (a1) and SCCM (b1) from −60° to 60°; RCS values of PEC and PEC coated with four different samples, respectively (c); comparison of RCS reduction values of PEC coated with four different samples (d).

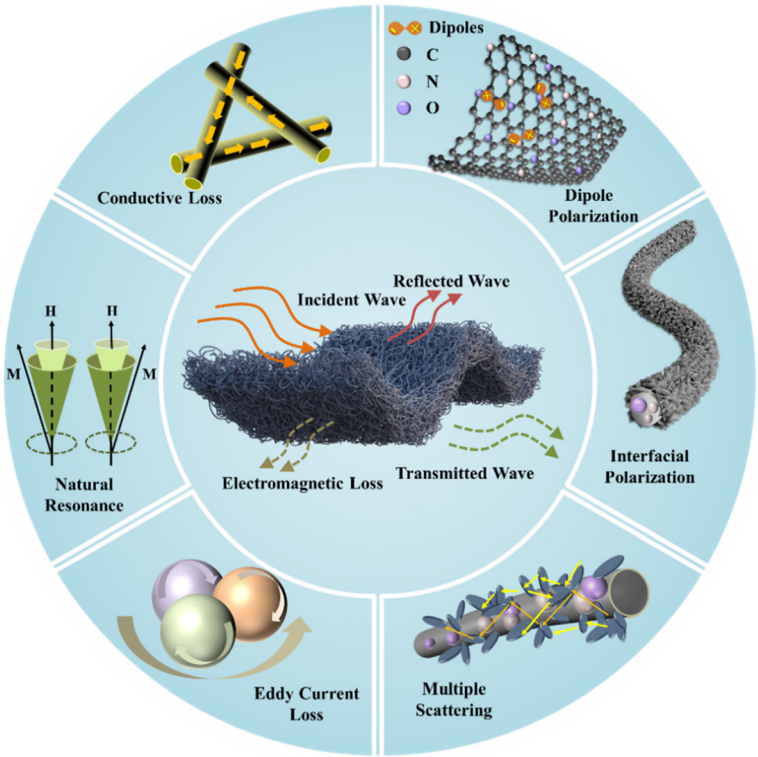

Fig. 7 Schematic diagram of potential electromagnetic loss mechanisms of SCCM.

between core and shell layers (MoS_2–CNF). Due to differences in electrical conductivity among these components, charge accumulated at the heterogeneous interfaces, resulting in significant interfacial polarization. Additionally, defects in the CNF (vacancies and N atom doping) and the MoS_2 nanosheets (Mo and S vacancies) increased dipole polarization sites, enriching relaxation losses. Second, the combined effect of MoS_2 slices with a high specific surface area and interwoven CNF forming 3D structures extended the microwave transmission path, enabling multiple reflection losses and promoting conductive losses. Finally, magnetic Co particles contributed to magnetic losses *via* natural resonance, exchange resonance, and eddy current loss, thereby improving the magnetic loss capacity of materials.

4. Conclusion

In conclusion, the SnCo/C@MoS_2 core–shell composite developed in this study demonstrated significant advancements in microwave absorption performance, driven by the synergy between 1D CNF and 2D MoS_2 nanosheets. By integrating the magnetic and conductive properties of SnCo with the dielectric properties of MoS_2, the composite achieved impressive RL (−64.27 dB), EAB (5.20 GHz) and RCS (below −20 dB m^2). The enhanced performance was attributed to a combination of interfacial polarization, dipole relaxation, conductive and magnetic losses, and the unique core–shell structure. This work underscores the potential of rationally designed 1D/2D hybrid architectures in developing lightweight, high-performance, and broadband microwave absorbers for practical EMW attenuation applications. Future work will explore scalability, long-term environmental stability, and integration into real-world EMW shielding systems.

Data availability

The authors confirm that the data supporting the findings of this study are available within the article and its ESI.†

Conflicts of interest

There are no conflicts to declare.

Acknowledgements

This research was funded by the Natural Science Foundation of Shandong Province (Grant No. ZR2021ME019).

References

1 X. Yang, L. Liang, C. Li, B. Zhang, Y. Zhao, S. Tan and G. Ji, Fluid-Actuated Nano-Micro-Macro Structure Morphing

Enables Smart Multispectrum Compatible Stealth, *Nano Lett.*, 2024, **25**(1), 569–577.
2 S. Zhang, S. Y. Zhang, P. Y. Zhu, J. Y. Li, Y. F. Li, C. L. Zhou, Q. Y. Qiu, X. Y. Jing, K. W. Paik and P. He, Recent achievements and performance of nanomaterials in microwave absorption and electromagnetic shielding, *Adv. Colloid Interface Sci.*, 2025, **335**, 103336.
3 X. Huang, J. Guan, Y. Feng, Q. Zhang, B. Quan, G. Shao, L. Gu, T. Guo, G. Sun and X. Zhu, Mn and O defect modulation in birnessite creates multiplicate polyhedra to improve dielectric and magnetic losses, *Cell Rep. Phys. Sci.*, 2025, **6**(1), 110235.
4 Y. Zhao, S. Tan, J. Yu, R. Yu, T. Xu, J. Zheng and G. Ji, A Rapidly Assembled and Camouflage–Monitoring–protection Integrated Modular Unit, *Adv. Mater.*, 2025, **37**(6), 2412845.
5 A. Shah, Y. Wang, H. Huang, L. Zhang, D. Wang, L. Zhou, Y. Duan, X. Dong and Z. Zhang, Microwave absorption and flexural properties of Fe nanoparticle/carbon fiber/epoxy resin composite plates, *Compos. Struct.*, 2015, **131**, 1132–1141.
6 Z. Fan, G. Luo, Z. Zhang, L. Zhou and F. Wei, Electromagnetic and microwave absorbing properties of multi-walled carbon nanotubes/polymer composites, *Mater. Sci. Eng., B*, 2006, **132**(1–2), 85–89.
7 F. Zheng, P. Wu, L. Wang, Y. Shi, J. Jiang, Y. Chen, Q. Zhuang, Q. Liu, Z. Ju and X. Kong, Activated Graphite with Richly Oxygenated Surface from Spent Lithium–Ion Batteries for Microwave Absorption, *Small*, 2025, 2409454.
8 F. Pan, L. Cai, Y. Dong, X. Zhu, Y. Shi and W. Lu, Mixed-dimensional hierarchical configuration of 2D Ni_2P nanosheets anchored on 1D silk-derived carbon fiber for extraordinary electromagnetic wave absorption, *J. Mater. Sci. Technol.*, 2022, **101**, 85–94.
9 X. Zhang, Y. Rao, J. Guo and G. Qin, Multiple-phase carbon-coated $FeSn_2$/Sn nanocomposites for high-frequency microwave absorption, *Carbon*, 2016, **96**, 972–979.
10 J. Hu, Z. Jiao, J. Jiang, Y. Hou, X. Su, J. Zhang, C. Feng, Y. Ma, M. Ma and J. Liu, Simple fabrication of cobalt-nickel alloy/carbon nanocomposite fibers for tunable microwave absorption, *J. Colloid Interface Sci.*, 2023, **652**, 1825–1835.
11 Y. Shen, Y. Wei, J. Ma, Y. Zhang, B. Ji, J. Tang, L. Zhang, P. Yan and X. Du, Self-cleaning functionalized FeNi/$NiFe_2O_4$/NiO/C nanofibers with enhanced microwave absorption performance, *Ceram. Int.*, 2020, **46**(9), 13397–13406.
12 W. J. Yu and G. F. Shao, Morphology engineering of defective graphene for microwave absorption, *J. Colloid Interface Sci.*, 2023, **640**, 680–687.
13 L. Zhang, X. Zhao, Y. Ma, Y. Shu, R. Zhang, J. Xiang, B. Wang, C. Mu, K. Zhai and T. Xue, Preparation and microwave absorption properties of tellurium doped black phosphorus nanoflakes and graphite nanoflakes composites, *J. Alloys Compd.*, 2023, **939**, 168700.
14 L. Xing, X. Li, Z. Wu, X. Yu, J. Liu, L. Wang, C. Cai, W. You, G. Chen and J. Ding, 3D hierarchical local heterojunction of MoS_2/FeS_2 for enhanced microwave absorption, *Chem. Eng. J.*, 2020, **379**, 122241.
15 F. Wu, Y. Xia, M. Sun and A. Xie, Two-dimensional (2D) few-layers WS_2 nanosheets: an ideal nanomaterials with tunable electromagnetic absorption performance, *Appl. Phys. Lett.*, 2018, **113**(5), 052906.
16 Y. Tong, M. He, Y. Zhou, X. Zhong, L. Fan, T. Huang, Q. Liao and Y. Wang, Electromagnetic wave absorption properties in the centimetre-band of $Ti_3C_2T_x$ MXenes with diverse etching time, *J. Mater. Sci.:Mater. Electron.*, 2018, **29**, 8078–8088.
17 W. Ye, F. Wu, N. Shi, H. Zhou, Q. Chi, W. Chen, S. Du, P. Gao, H. Li and S. Xiong, Metal-semiconductor phase twinned hierarchical MoS_2 nanowires with expanded interlayers for sodium–ion batteries with ultralong cycle life, *Small*, 2020, **16**(3), 1906607.
18 J. Wang, X. Lin, Z. Chu, Z. Huang, T. Guo, L. Yang and S. Li, Magnetic MoS_2: a promising microwave absorption material with both dielectric loss and magnetic loss properties, *Nanotechnology*, 2020, **31**(13), 135602.
19 Y. Sun, W. Zhong, Y. Wang, X. Xu, T. Wang, L. Wu and Y. Du, MoS_2-based mixed-dimensional van der Waals heterostructures: a new platform for excellent and controllable microwave-absorption performance, *ACS Appl. Mater. Interfaces*, 2017, **9**(39), 34243–34255.
20 L. Xu, J. Tao, X. Zhang, Z. Yao, B. Wei, F. Yang, C. Zhou, A. Zavabeti, K. Zuraiqi and J. Zhou, Hollow C@MoS_2 nanospheres for microwave absorption, *ACS Appl. Nano Mater.*, 2021, **4**(10), 11199–11209.
21 X. Zhao, Y. Huang, X. Liu, M. Yu, M. Zong and T. Li, Magnetic nanorods/carbon fibers heterostructures coated with flower-like MoS_2 layers for superior microwave absorption, *Carbon*, 2023, **213**, 118265.
22 Z. Guo, D. Lan, C. Zhang, Z. Gao, M. Han, X. Shi, M. He, H. Guo, Z. Jia and G. Wu, "Two birds one stone" strategy to integrate electromagnetic wave absorption and self-anticorrosion in magnetic nanocomposites with double-shell hollow structure, *J. Mater. Sci. Technol.*, 2025, **220**, 307–319.
23 K. Luo, C. Xu, Y. Du, X. Lv, X. Yang, M. Liu, W. Zhao, C. Zhang, Y. Lai and Z. Liu, Multidimensional Engineering Induced Interfacial Polarization by in–Situ Confined Growth of MoS_2 Nanosheets for Enhanced Microwave Absorption, *Small*, 2024, **20**(44), 2402729.
24 S. Zhang, C. Xiong, J. H. Yin, H. T. Sun, Z. Y. Qi, H. Y. Deng and K. B. Cui, Microwave absorption properties of Co/C and Ni/C composite nanofibers prepared by electrospinning, *Mater. Res. Express*, 2024, **11**(9), 095003.
25 M. Zhang, R. Zhu, C. Qian, J. Wang, Z. Jin, Y. Zhang, W. Zhang and Q. Liu, Facile synthesis of 2D MoS_2/reduced graphene oxide hybrids with excellent microwave absorption, *J. Alloys Compd.*, 2023, **953**, 170005.
26 S. Dong, J. Li, N. Li, S. Zhang, B. Li, Q. Zhang and L. Ge, Enhanced broadband microwave absorption of Fe/C core-shell nanofibers in X and Ku bands, *Ceram. Int.*, 2023, **49**(5), 8181–8189.

27 X. Kong, J. Xu, Z. Ju and C. Chen, Durable Ru nanocrystal with HfO_2 modification for acidic overall water splitting, *Nano-Micro Lett.*, 2024, **16**(1), 185.
28 P. Wang, L. F. Cheng, Y. Zhang, W. Y. Yuan, H. X. Pan and H. Wu, Electrospinning of graphite/SiC hybrid nanowires with tunable dielectric and microwave absorption characteristics, *Composites, Part A*, 2018, **104**, 68–80.
29 W. Hu, M. Zhou and H. Fu, Impedance matching optimization of hierarchical carbon fiber@ MoS_2@PANI nanocomposite with core–sheath structure for achieving excellent microwave absorption, *Polym. Adv. Technol.*, 2023, **34**(11), 3644–3654.
30 M. Ma, Q. Zheng, Y. Zhu, L. Li and M. Cao, Confinedly implanting Fe_3O_4 nanoclusters on MoS_2 nanosheets to tailor electromagnetic properties for excellent multi-bands microwave absorption, *J. Mater.*, 2022, **8**(3), 577–585.
31 J. Ma, H. Ren, Z. Liu, J. Zhou, Y. Wang, B. Hu, Y. Liu, L. B. Kong and T. Zhang, Embedded MoS_2-PANI nanocomposites with advanced microwave absorption performance, *Compos. Sci. Technol.*, 2020, **198**, 108239.
32 S. H. Shi, P. P. Mou, D. Wang, X. Y. Li, S. J. Teng, M. F. Zhou, X. L. Yu, Z. Deng, G. P. Wan and G. Z. Wang, Co/carbon nanofiber with adjustable size and content of Co nanoparticles for tunable microwave absorption and thermal conductivity, *J. Mater.*, 2024, **10**(1), 124–133.
33 T.-B. Geng, G.-Y. Yu, G.-F. Shao and X.-G. Huang, Enhanced electromagnetic wave absorption properties of ZIF-67 modified polymer-derived SiCN ceramics by in situ construction of multiple heterointerfaces, *Rare Met.*, 2023, **42**(5), 1635–1644.
34 F. Hu, P. Zhang, F. Wu, Z. Tian, H. Tang, B. Fan, R. Zhang, W. Sun, L. Cai and Z. M. Sun, One-dimensional core-sheath Sn/SnO_x derived from MAX phase for microwave absorption, *J. Mater.*, 2024, **10**(3), 531–542.
35 J. Cui, X. H. Wang, L. Huang, C. W. Zhang, Y. Yuan and Y. B. Li, Environmentally friendly bark-derived Co-Doped porous carbon composites for microwave absorption, *Carbon*, 2022, **187**, 115–125.
36 L. G. Cheng, Q. W. Wang and J. Ding, Synthesis of Co/CoO@RGO composite for enhanced electromagnetic microwave absorption performance, *Appl. Phys. A:Mater. Sci. Process.*, 2021, **127**(1), 041830.
37 L. L. Xing, H. R. Cheng, Y. Li, Q. Chen, C. T. Liu, C. Y. Shen and X. H. Liu, MoS_2 Decorated on 1D MoS_2@Co/NC@CF Hierarchical Fibrous Membranes for Enhanced Microwave Absorption, *Small*, 2025, **21**(1), 2407337.
38 M. Wu, X. Liang, Y. Zheng, C. Qian and D. Wang, Excellent microwave absorption performances achieved by optimizing core@shell structures of Fe_3O_4@1T/2H-MoS_2 composites, *J. Alloys Compd.*, 2022, **910**, 164881.
39 S. Liu, D. Fang, F. Xing, H. Jin and J. Li, Auricularia-shaped MoS_2 nanosheet arrays coated hierarchical multilayer MoS_2/PPy/rGO composites for efficient microwave absorption, *Chem. Eng. J.*, 2024, **479**, 147613.
40 X. Tian, Y. Wang, J. Wang, Z. Guo, L. Hu, C. Tang, G. Chen and Y. Fang, One–Pot Hydrothermal Synthesis of Core-Shell MnS@MoS_2 Heterojunction for Enhanced Microwave Absorption, *Adv. Eng. Mater.*, 2023, **25**(9), 2201526.
41 W. Zhu, L. Zhang, W. Zhang, F. Zhang, Z. Li, Q. Zhu and S. Qi, Facile synthesis of GNPs@ NixSy@MoS_2 composites with hierarchical structures for microwave absorption, *Nanomaterials*, 2019, **9**(10), 1403.
42 H. Zhao, Y. Cheng, Z. Zhang, J. Yu, J. Zheng, M. Zhou, L. Zhou, B. Zhang and G. Ji, Rational design of core-shell Co@C nanotubes towards lightweight and high-efficiency microwave absorption, *Composites, Part B*, 2020, **196**, 108119.
43 Z. Liao, M. Ma, Y. Bi, Z. Tong, K. L. Chung, Z. Li, Y. Ma, B. Gao, Z. Cao, R. Sun and X. Zhong, MoS2 decorated on one-dimensional $MgFe_2O_4$/MgO/C composites for high-performance microwave absorption, *J. Colloid Interface Sci.*, 2022, **606**, 709–718.
44 X. Kong, P. Wu, S. Tian, T. Chen, S. Zhao, Q. Liu and Z. Ju, All-in-one: Multi-parameter engineering on γ-Fe_2O_3 for ultra-broadband microwave absorption, *Chem. Eng. J.*, 2024, **485**, 150144.
45 R. Rohini and S. Bose, Electromagnetic wave suppressors derived from crosslinked polymer composites containing functional particles: Potential and key challenges, *Nano-Struct. Nano-Objects*, 2017, **12**, 130–146.
46 X. Zhao, Y. Huang, X. Liu, J. Yan, L. Ding, M. Zong, P. Liu and T. Li, Core-shell $CoFe_2O_4$@ C nanoparticles coupled with rGO for strong wideband microwave absorption, *J. Colloid Interface Sci.*, 2022, **607**, 192–202.
47 J. Zhang, X. Qi, X. Gong, Q. Peng, Y. Chen, R. Xie and W. Zhong, Microstructure optimization of core@ shell structured MSe_2/$FeSe_2$@ $MoSe_2$ (M= Co, Ni) flower-like multicomponent nanocomposites towards high-efficiency microwave absorption, *J. Mater. Sci. Technol.*, 2022, **128**, 59–70.
48 H. Geng, X. Zhang, W. Xie, P. Zhao, G. Wang, J. Liao and L. Dong, Lightweight and broadband 2D MoS_2 nanosheets/3D carbon nanofibers hybrid aerogel for high-efficiency microwave absorption, *J. Colloid Interface Sci.*, 2022, **609**, 33–42.
49 Y. Zhang, Y.-Y. Xie, W.-T. Yang, G. Wu, S.-C. Chen and Y.-Z. Wang, Multidimensional and hierarchical design of biomass-derived carbon nanofiber networks for efficient microwave absorption, *Colloids Surf., A*, 2024, **696**, 134270.
50 Y. Liu, C. Ji, X. Su, X. He, J. Xu and Y. Li, Enhanced microwave absorption properties of flaky MoS_2 powders by decorating with Ni particles, *J. Magn. Magn. Mater.*, 2020, **511**, 166961.
51 R. Xue, R. Qiang, Y. Shao, X. Yang, Q. Ma, Y. Chen, F. Ren, Y. Ding, B. Chen and S. Feng, MoS2-Decorated Tubular Carbon Nanostructures with Enhanced Dielectric Loss for Boosting Microwave Absorption, *ACS Appl. Nano Mater.*, 2024, 7(14), 16075–16085.
52 X. Sun, X. Li, P. Chen and Y. Zhu, Construction of urchin-like multiple core-shelled Co/CoS_2@ NC@ MoS_2 composites for effective microwave absorption, *J. Alloys Compd.*, 2023, **936**, 168243.

53 Y. Bi, M. Ma, Y. Liu, Z. Tong, R. Wang, K. L. Chung, A. Ma, G. Wu, Y. Ma, C. He, P. Liu and L. Hu, Microwave absorption enhancement of 2-dimensional CoZn/C@MoS_2@PPy composites derived from metal-organic framework, *J. Colloid Interface Sci.*, 2021, **600**, 209–218.
54 X. Lin, J. Wang, Z. Chu, D. Liu, T. Guo, L. Yang, Z. Huang, S. Mu and S. Li, The optimization of hydrothermal process of MoS_2 nanosheets and their good microwave absorption performances, *Chin. Chem. Lett.*, 2020, **31**(5), 1124–1128.
55 M. Acerce, D. Voiry and M. Chhowalla, Metallic 1T Phase MoS_2 Nanosheets as SupercapacitorElectrode Materials, *Nat. Nanotechnol.*, 2015, **10**, 313.
56 F. Hu, J. Dai, Q. Liu, Z. Zhang and G. Xu, Synthesis of Flowerlike MoS_2/CoNi Composites for Enhancing Electromagnetic Wave Absorption, *Acta Metall. Sin. (Engl. Lett.)*, 2022, 1–11.
57 C. Wang, Y. Liu, Z. Jia, W. Zhao and G. Wu, Multicomponent nanoparticles synergistic one-dimensional nanofibers as heterostructure absorbers for tunable and efficient microwave absorption, *Nano-Micro Lett.*, 2023, **15**(1), 13.
58 C. Li, L. Liang, B. Zhang, Y. Yang and G. Ji, Magneto-dielectric synergy and multiscale hierarchical structure design enable flexible multipurpose microwave absorption and infrared stealth compatibility, *Nano-Micro Lett.*, 2025, **17**(1), 1–16.
59 W. Wang, K. Nan, H. Zheng, Q. Li and Y. Wang, Heterostructure design of hydrangea-like Co_2P/Ni_2P@C multilayered hollow microspheres for high-efficiency microwave absorption, *J. Mater. Sci. Technol.*, 2024, **181**, 104–114.
60 C. Han, M. Zhang, W.-Q. Cao and M.-S. Cao, Electrospinning and *in situ* hierarchical thermal treatment to tailor C-$NiCo_2O_4$ nanofibers for tunable microwave absorption, *Carbon*, 2021, **171**, 953–962.
61 J. Liu, Z. Jia, W. Zhou, X. Liu, C. Zhang, B. Xu and G. Wu, Self-assembled MoS_2/magnetic ferrite $CuFe_2O_4$ nanocomposite for high-efficiency microwave absorption, *Chem. Eng. J.*, 2022, **429**, 132253.
62 Y. Hui-Jing, C. Wen-Qiang, Z. De-Qing, S. Tie-Jian, S. Hong-Long, W. Wen-Zhong, Y. Jie and C. Mao-Sheng, NiO Hierarchical Nanorings on SiC: Enhancing Relaxation to Tune Microwave Absorption at Elevated Temperature, *ACS Appl. Mater. Interfaces*, 2015, 7073–7077.
63 X. Huang, G. Yu, B. Quan, J. Xu, G. Sun, G. Shao, Q. Zhang, T. Guo, J. Guan and M. Zhang, Harnessing Pseudo–Jahn-Teller Disordering of Monoclinic Birnessite for Excited Interfacial Polarization and Local Magnetic Domains, *Small Methods*, 2023, **7**(9), 2300045.
64 P. Wu, X. Kong, Y. Feng, W. Ding, Z. Sheng, Q. Liu and G. Ji, Phase engineering on amorphous/crystalline γ–Fe_2O_3 nanosheets for boosting dielectric loss and high–performance microwave absorption, *Adv. Funct. Mater.*, 2024, **34**(10), 2311983.
65 B. Lu, X. L. Dong, H. Huang, X. F. Zhang, X. G. Zhu, J. P. Lei and J. P. Sun, Microwave absorption properties of the core/shell-type iron and nickel nanoparticles, *J. Magn. Magn. Mater.*, 2008, **320**(6), 1106–1111.
66 S. Gao, G. Zhang, Y. Wang, X. Han, Y. Huang and P. Liu, MOFs derived magnetic porous carbon microspheres constructed by core-shell Ni@C with high-performance microwave absorption, *J. Mater. Sci. Technol.*, 2021, **88**, 56–65.
67 R. Guo, D. Su, K. Zou, C. Zhang, F. Cen, H. Luo, F. Chen and S. Jiang, N-Doped, Carbon Fibers with Embedded ZnFe and Fe_3C Nanoparticles for Microwave Absorption, *ACS Appl. Nano Mater.*, 2021, **4**(10), 11070–11079.
68 Z. Zhang, Y. Zhao, Z. Li, L. Zhang, Z. Liu, Z. Long, Y. Li, Y. Liu, R. Fan and K. Sun, Synthesis of carbon/SiO_2 core-sheath nanofibers with Co-Fe nanoparticles embedded in via electrospinning for high-performance microwave absorption, *Adv. Compos. Hybrid Mater.*, 2022, 1–12.
69 W. Huang, Z. Tong, Y. Bi, M. Ma, Z. Liao, G. Wu, Y. Ma, S. Guo, X. Jiang and X. Liu, Synthesis and microwave absorption properties of coralloid core-shell structure NiS/Ni_3S_4@PPy@MoS_2 nanowires, *J. Colloid Interface Sci.*, 2021, **599**, 262–270.
70 R. Xue, D. Lan, R. Qiang, Z. Zang, J. Ren, Y. Shao, L. Rong, J. Gu, J. Fang and G. Wu, Synergistic dielectric regulation strategy of one-dimensional MoO_2/Mo_2C/C heterogeneous nanowires for electromagnetic wave absorption, *Carbon*, 2025, **233**, 119877.
71 G. Yu, G. Shao, R. Xu, Y. Chen, X. Zhu and X. Huang, Metal-organic framework–manipulated dielectric genes inside silicon carbonitride toward tunable electromagnetic wave absorption, *Small*, 2023, **19**(46), 2304694.
72 C. Liu, T. He, C. Hu, Q. Qian, Y. Hao, L. Xu, H. Lu and G. Ji, The optimized design of sandwich structured SiO_2/C@SiC/SiO_2 composites through numerical simulation for temperature–resistant radar and infrared compatible stealth, *Adv. Funct. Mater.*, 2025, **35**(9), 2416108.
73 Q. Li, K. Nan, W. Wang, H. Zheng and Y. Wang, Electrostatic self-assembly sandwich-like 2D/2D NiFe-LDH/MXene heterostructure for strong microwave absorption, *J. Colloid Interface Sci.*, 2023, **648**, 983–993.